Journal of ELECTRONIC MATERIALS, Vol. 48, No. 9, 2019
https://doi.org/10.1007/s11664-019-06925-0

A Low-Power Thermoelectric Energy Harvesting System for High Internal Resistance Thermoelectric Generators

KUNPENG WANG,[1] MINGJIE GUAN,[2] FU CHEN,[2] and WEI-HSIN LIAO [1,3]

1.—Department of Mechanical and Automation Engineering, The Chinese University of Hong Kong, Shatin, N.T., Hong Kong, China. 2.—School of Aerospace Engineering, Xiamen University, Xiamen, Fujian, China. 3.—e-mail: whliao@cuhk.edu.hk

This paper presents an energy harvesting system targeted to harness energy from a high internal resistance thermoelectric generator (TEG) under low temperature difference condition. The system is based on a DC–DC boost converter with a maximum power point tracking scheme. An optimal current control scheme and zero current switching technique are applied for low power consumption and high efficiency. An analysis on power losses of the system is performed. A prototype system is built to show the performance and to verify the theoretical analysis. Experimental results show that the proposed system can harvest enough power to run a wireless sensor node at a transmission cycle of 30 s with a minimum input power of 27 μW and a low temperature difference of 1.9 K across the TEG. The peak efficiency of the power conversion can reach 75.2% in the considered input voltage range.

Key words: Boost converter, DC–DC converter, maximum power point tracking, thermal energy harvesting, zero current switching

INTRODUCTION

The emergence of wireless sensor networks (WSNs) and their widespread use have highlighted a challenge: In many applications it is difficult to obtain physical access to replace or recharge the batteries of the sensor nodes. Thanks for the advances in power electronics, the power required for the WSN nodes has been decreased to several microwatts. Therefore, powering a WSN node by using an energy harvester becomes attractive. Thermal energy harvesting is a promising energy harvesting technology. With the improvement of the efficiency of thermoelectric generator (TEG), harvesting ambient heat energy seems to be a convenient means to supply power for WSN nodes. Romanjek et al.[1] applied high-performance thermoelectric modules array for gas exhaust energy scavenging. When the temperature difference was increased to 500 K, electrical power output increased to above 3.6 W. Dilhac et al.[2] implemented thermoelectric energy harvesting system in airliners to power battery-free WSNs; however, the temperature difference must be maintained above 20 K to generate enough energy for WSNs.

In natural convection environment, the temperature difference of the TEG cannot be kept high due to the homogenization process, especially when the TEG is used to harvest the thermal energy from the human body. Moritz et al.[3] proposed to determine the thermal potential of the human body. The maximum power that could be produced by TEG can reach microwatts per square centimeter of covered skin. Deng et al.[4] explored some experiments of wearable TEG at different locations on the human body. The maximum obtained power of a single TEG module can reach about 50 μW at an ambient temperature of 21°C, but the open circuit voltage is only about 40 mV. As the voltage produced by TEG is usually low, one approach is to use a high-ratio converter to boost the generated voltage into a high output voltage. In the work by Krishna

(Received October 27, 2018; accepted January 3, 2019; published online January 14, 2019)

et al.,[5] they designed a TEG system for body energy harvesting with the consideration of a boost converter; however, the peak efficiency is only 30% due to the high conversion ratio. To tackle this issue, Guan et al.[6] proposed a high efficiency boost converter for a low-voltage thermoelectric energy harvesting system. The presented boost converter with a maximum power point tracking (MPPT) scheme can achieve a higher efficiency than the commercial solution in the considered voltage range. However, the designed output voltage of the converter is 1.5 V, which is not high enough to meet the demand of a WSN node. They also implemented a two-stage high-ratio converter to boost the output voltage to more than 2.6 V to power the WSN nodes.[7] The converter efficiency ranges from 44.2% to 75.4% in the 84–400 mV open-circuit voltage range with a regulated output voltage of 2.3 V. As high-ratio is undesired for high efficiency of the converter, one approach is to connect more thermal couples in series to increase the output voltage of the TEG element. A miniature TEG element with more thermal couples and higher power density has been developed.[8] It is shown that the open circuit voltage and internal resistance of the TEG increase substantially regarding the same temperature difference compared to the conventional TEG.[9] For the high-internal-resistance TEG, a boost converter designed towards high internal resistance TEG is needed. Moreover, TEGs are often employed in environments with time-varying temperature differences. Therefore, it is necessary to control the converter with a MPPT algorithm. Several circuit topologies have been proposed for high internal resistance power source with MPPT scheme.[10,11] A transformer-based boost converter was designed and demonstrated for high internal resistance power source.[10] However, its efficiency is too low when the input voltage is lower than 200 mV. A boost converter with a cascaded capacitor-less low drop-out voltage regulator was developed for high internal resistance voltage source.[11] However, the maximum input voltage of the converter is as low as 200 mV. There are some commercially available boost converters. Texas Instruments released a low-power boost converter chip BQ25504 for energy harvesting.[12] However, the efficiency of the converter at low input current is low. A commercial boost converter[13] can boost from a low voltage of 20 mV. But it does not possess a MPPT ability and has a low input resistance of several ohms.

The main work of this paper is to design a thermoelectric energy harvesting system to power wireless sensor nodes with high internal resistance TEG under low temperature difference condition. A MPPT scheme, a peak current control scheme and a zero current switch (ZCS) control technique are implemented to achieve a high efficiency. Sources of power loss are analyzed. A thermoelectric energy harvesting prototype is built. The performance of the proposed system is tested.

The rest of the paper is organized as follows. In "System Description" section, the proposed system is introduced. "Circuit Architecture and Design Techniques" section describes the MPPT and ZCS schemes for the proposed system. In "Current Control Scheme" section, the power dissipation sources are analyzed, and an optimal inductor current control scheme is described. "Experiments" section presents the experiments and the measurement results. "Conclusions" section concludes the paper.

SYSTEM DESCRIPTION

A thermoelectric energy harvesting system integrated with a WSN node is comprised of four subsystems as shown is Fig. 1. It includes a TEG for power generation, a DC–DC converter for voltage conversion, a WSN node for transmission, and a power management unit to run the WSN node and store extra energy in a reservoir.

Thermoelectric Generator

A TEG is a device that can directly convert temperature difference into electricity. Typically, it can be regarded as a voltage source V_T in series with an internal resistance R_T. The maximum power can be extracted when the external load is equal to the internal resistor R_T. The maximum output power is

$$P_{max} = \frac{V_T^2}{4R_T} \quad (1)$$

DC–DC Converter

In this paper, an inductor-based converter is adopted. As shown in Fig. 2, it consists of two switches G_1, G_2, an inductor L_0, an input capacitor C_{in} and an output capacitor C_{out}. In this paper, a discontinuous mode (DCM) is adopted to lower the switching frequency and the switching loss of the system.

Power Management Unit and WSN Node

The power management unit is to regulate the voltage to the WSN node and transfer the extra output energy to a reservoir (a supercapacitor). An EZ430-RF2500 tool kit[14] is adopted in this paper. The power dissipation of a WSN node varies from several microwatts to several milliwatts depending on the transmission frequency.

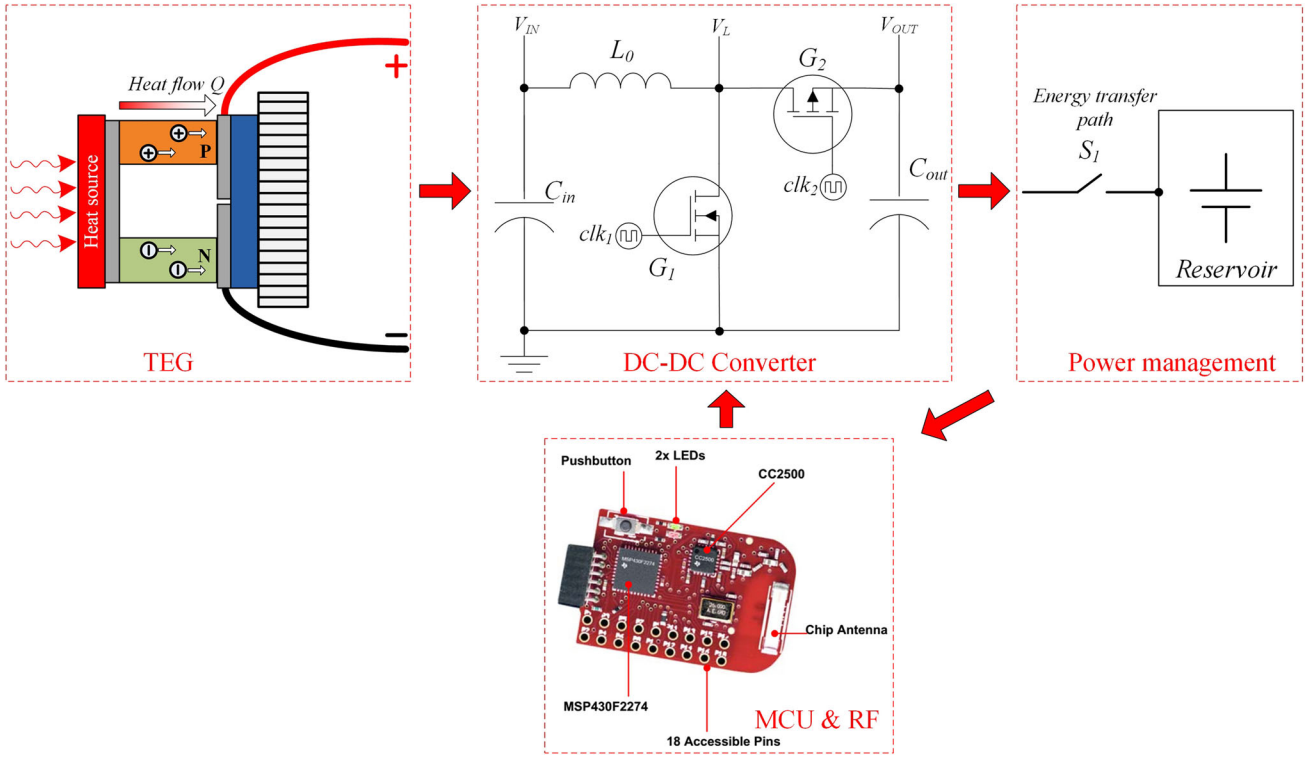

Fig. 1. Overview of the thermoelectric energy harvesting system integrated with the wireless sensor node.

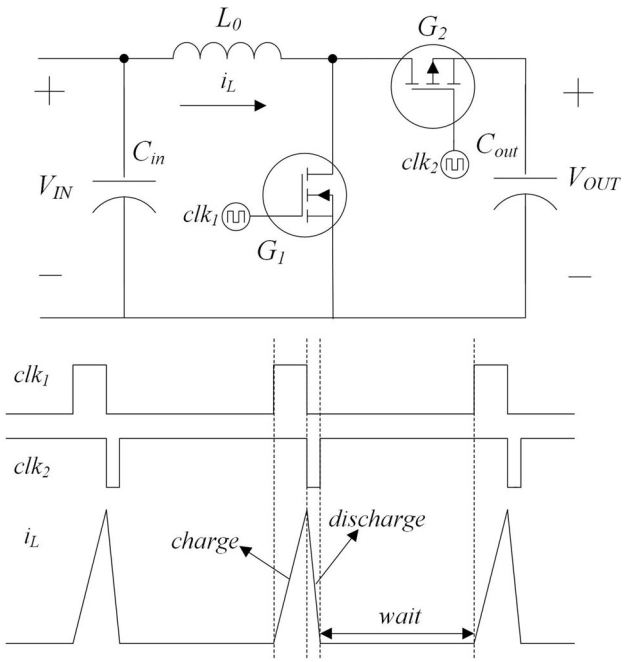

Fig. 2. Basic topology and operation mode of the boost converter.

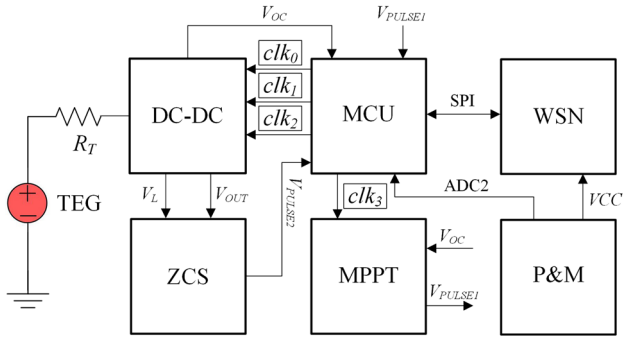

Fig. 3. Diagram of the power management circuit for TEG harvester.

CIRCUIT ARCHITECTURE AND DESIGN TECHNIQUES

Overall Architecture of the Proposed Circuit System

The proposed architecture of energy harvesting system is illustrated in Fig. 3. The system consists of a control unit integrated with a WSN node, a DC–DC module, a ZCS module, a MPPT module and a power management module to provide stable power supply

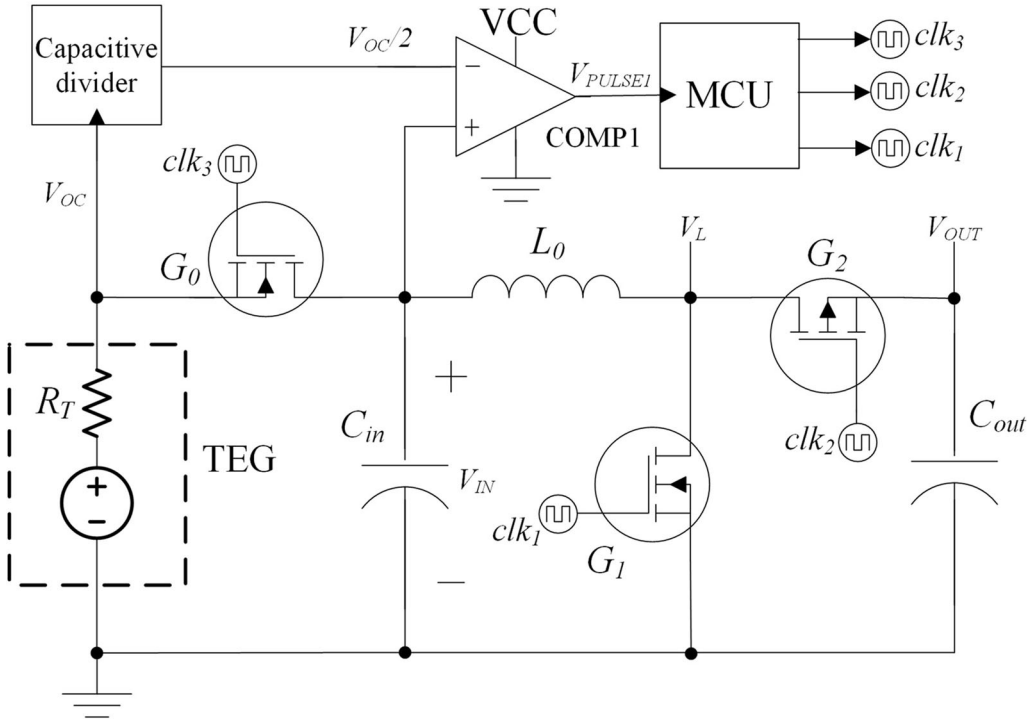

Fig. 4. Circuit topology of the MPPT block of boost converter.

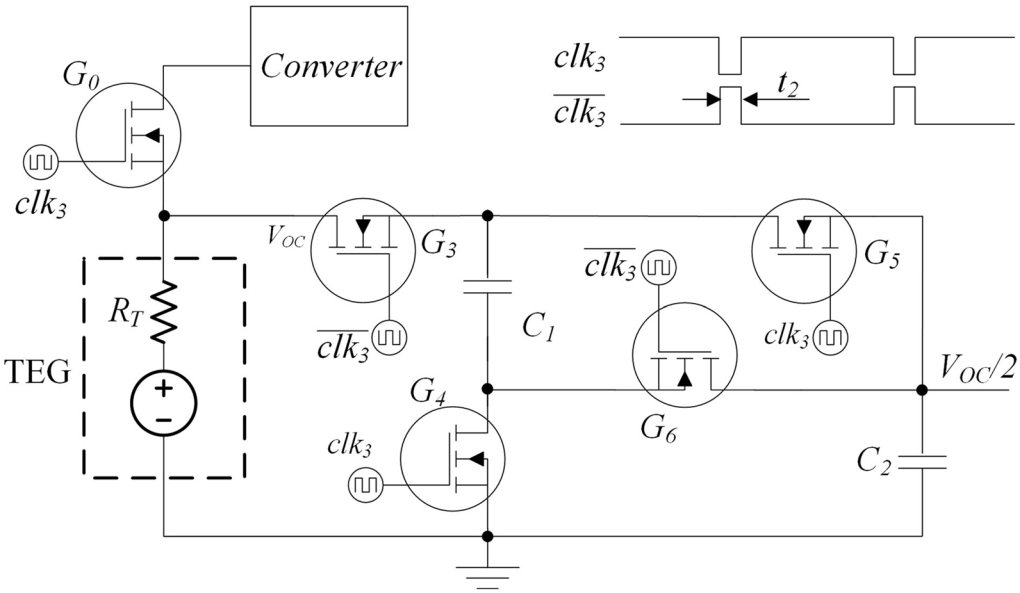

Fig. 5. An improved capacitive divider topology.

to the load. The details of design techniques in each module are explained in the following sections.

Maximum Power Extraction Based on DC–DC Converter

The TEG generator has a high internal resistance. Under low temperature difference conditions, the output current of the TEG generator is extremely low. This section presents the boost converter with MPPT mechanism to achieve an impedance match and convert the extremely low input current to a high voltage. The boost converter and MPPT module is shown in Fig. 4. It is mainly comprised of a voltage comparator COMP1, MCU and a capacitive divider that is responsible to obtain half value

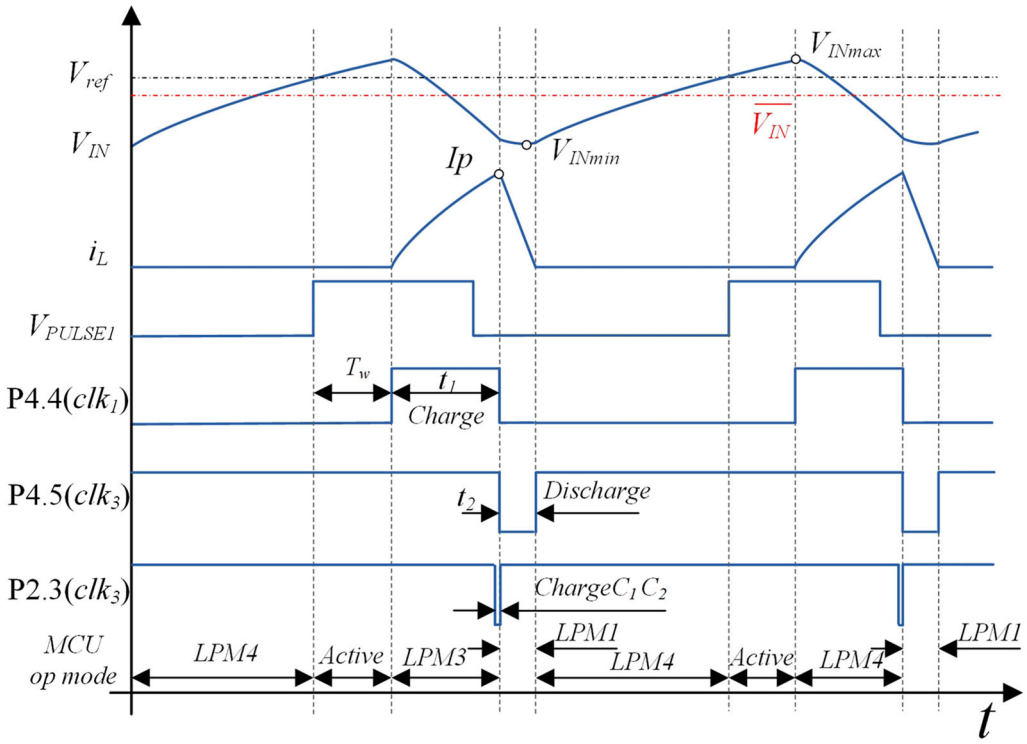

Fig. 6. Waveforms explaining the operation of MPPT scheme.

of the open-circuit voltage for reference. The topology structure and operating principle of the capacitive divider shown in Fig. 5.

A timing diagram for the operation is provided in Fig. 6 to explain the MPPT scheme. When the voltage of input capacitor C_{in} reaches the half of V_{OC}, a pulse signal V_{PULSE1} generated by COMP1 goes high to trigger MCU to start the boost conversion. When the boost conversion starts, the switch G_1 is turned on to transfer energy from input capacitor to inductor L_0 for a certain time, which causes the voltage of input capacitor C_{in} decreases and V_{PULSE1} goes down. And then the switch G_1 is turned off and switch G_2 is turned on to let the inductor L_0 discharge. Finally, the switch G_2 is turned off and the boost circuit enters the "Wait" phase. The boost converter starts the next conversion procedure until the input voltage reaches half of V_{OC} again.

For low power consumption purpose, MCU changes its operating mode according to the operating state of the converter. For most of the time, MCU works under low-power-mode 4 (LPM4) and low-power-mode 3 (LPM3), resulting in an average power consumption as low as several microwatts. Figure 7 is a flow chart of the MPPT scheme implemented with the MSP430 microcontroller.

ZCS Technique

As shown in Fig. 4, a PMOS switch G_2 is adopted instead of a diode in a conventional boost converter to reduce the voltage drop across the diode. The switch G_2 is controlled by signal clk_2, and the width of the low level of signal clk_2 is marked as t_2. ZCS is fulfilled by turning off the switch G_2 when the current i_L decreases to zero. If the parameter t_2 is too short or too long, the switch G_2 may not work under ZCS mode. As shown in Fig. 8, there is unnecessary power consumption when the switch G_2 is turned off too early or too late. Theoretically, the optimal parameter t_2 can be approximately calculated by

$$t_2 = t_1 \cdot \frac{V_{\text{IN}}}{V_{\text{OUT}} - V_{\text{IN}}} \tag{2}$$

From Eq. 2, it can be found that the appropriate time interval t_2 is related to the time interval t_1, voltage V_{IN} and voltage V_{OUT}. These parameters are varying and the appropriate t_2 should be varying too to achieve ZCS. In this paper, ZCS is achieved by dynamically determining parameter t_2 from detecting the voltage on node V_{L} right after the switch G_2 is turned off.

The circuit diagram of the ZCS block to dynamically determine the time t_2 is illustrated in Fig. 9. A low power comparator is needed to compare the voltages V_{L} and V_{OUT} after the switch G_2 is turned off. A capture block is used to detect the voltage output signal from comparator to dynamically adjust t_2. The operation procedure and waveforms are also shown in Fig. 9. The corresponding flow chart for ZCS algorithm is illustrated in Fig. 10. The

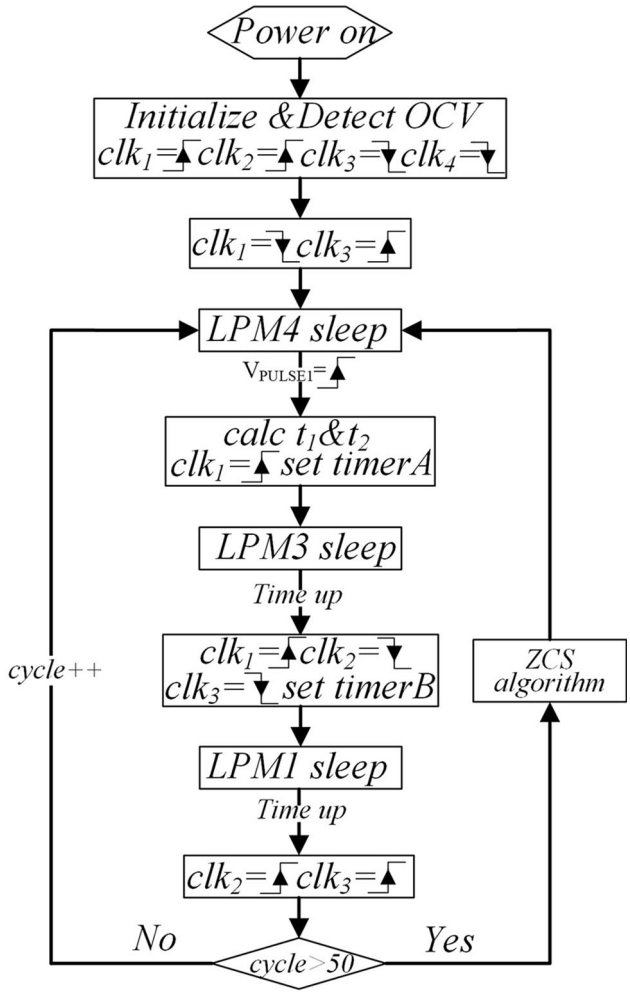

Fig. 7. Flow chart diagram of the boost conversion loop.

operating cycle can be adjusted by software to fulfill a quick determination of time t_2.

Power Management Strategy

The simplified circuit diagram of the PMU is shown in Fig. 11a. The detailed circuit diagram of the PMU is illustrated in Fig. 11c, which consists of a comparator, three MOSFETs and several resistors. When the output energy in capacitor C_{out} exceeds the need of the load, the extra energy is transferred to a supercapacitor. On the other hand, when the output energy is not enough for the load, the load will consume the power from the supercapacitor. In addition, PMU must prevent the supercapacitor from being deeply discharged or overcharged. As shown in Fig. 11b, a high threshold voltage V_{OV} to prevent the supercapacitor from over-charged and a low threshold voltage V_{UV} to avoid over-discharged are set. A hysteresis voltage V_{HYST} is set to create a hysteresis loop.

CURRENT CONTROL SCHEME

A theoretical power loss analysis and an optimal current control scheme on boost converter based on the power loss analysis are given in this section.

Power Loss Analysis of the Converter and MCU

The total energy loss in the circuit is given as

$$P_{\mathrm{Loss}} = P_{\mathrm{CN}} + P_{\mathrm{SW}} + P_{\mathrm{CU}} \tag{3}$$

where P_{CN} is the conduction loss, P_{SW} is the switching loss, and P_{CU} is the energy loss of the control unit.

P_{CN} consists of two parts, $P_{\mathrm{CN,charge}}$ and $P_{\mathrm{CN,discharge}}$, representing charge and discharge conduction loss, respectively. To simplify the derivation, it is considered that the current in the inductor increases with time in the interval t_1, there is

$$\frac{\Delta i_{\mathrm{L}}}{t_1} = \frac{V_{\mathrm{IN}} - i_{\mathrm{L}}(R_{\mathrm{L}} + R_{\mathrm{on1}})}{L} \tag{4}$$

where L is the inductance of the inductor in the converter; R_{L} is the resistance of inductor; R_{on1} is the resistance of switch G_1 when G_1 is turned on.

During the charge time t_1, the conductive energy loss in one cycle is

$$E_{\mathrm{CN,charge}} = \int_0^{t_1} i_{\mathrm{L}}^2 (R_{\mathrm{L}} + R_{\mathrm{on1}}) \mathrm{d}t \tag{5}$$

Rewriting Eq. 5 to a current integral using Eq. 4, there is

$$E_{\mathrm{CN,charge}} = \int_0^{I_{\mathrm{p}}} i_{\mathrm{L}}^2 (R_{\mathrm{L}} + R_{\mathrm{on1}}) \frac{L}{V_{\mathrm{IN}} - i_{\mathrm{L}} R_{\mathrm{L}} - i_{\mathrm{L}} R_{\mathrm{on1}}} \mathrm{d}i_{\mathrm{L}} \tag{6}$$

where I_{p} is the peak current reached at $t = t_1$.

As $i_{\mathrm{L}}(R_{\mathrm{L}} + R_{\mathrm{on1}})$ is much smaller than V_{IN}, there is

$$\begin{aligned} E_{\mathrm{CN,charge}} &= \int_0^{I_{\mathrm{p}}} i_{\mathrm{L}}^2 (R_{\mathrm{L}} + R_{\mathrm{on1}}) \frac{L}{V_{\mathrm{IN}}} \mathrm{d}i_{\mathrm{L}} \\ &= \frac{I_{\mathrm{p}}^3 L (R_{\mathrm{L}} + R_{\mathrm{on1}})}{3 V_{\mathrm{IN}}} \end{aligned} \tag{7}$$

Similarly, the conduction loss of discharge phase in one operation cycle is obtained as

$$\begin{aligned} E_{\mathrm{CN,discharge}} &= \int_0^{I_{\mathrm{p}}} i_{\mathrm{L}}^2 (R_{\mathrm{L}} + R_{\mathrm{on2}}) \frac{L}{V_{\mathrm{OUT}} - V_{\mathrm{IN}}} \mathrm{d}i_{\mathrm{L}} \\ &= \frac{I_{\mathrm{p}}^3 L (R_{\mathrm{L}} + R_{\mathrm{on2}})}{3(V_{\mathrm{out}} - V_{\mathrm{IN}})} \end{aligned} \tag{8}$$

Finally, the total conduction energy dissipation is

$$P_{\mathrm{CN}} = f \cdot \left[\frac{I_{\mathrm{p}}^3 L (R_{\mathrm{L}} + R_{\mathrm{on1}})}{3 V_{\mathrm{in}}} + \frac{I_{\mathrm{p}}^3 L (R_{\mathrm{L}} + R_{\mathrm{on2}})}{3(V_{\mathrm{OUT}} - V_{\mathrm{in}})} \right] \tag{9}$$

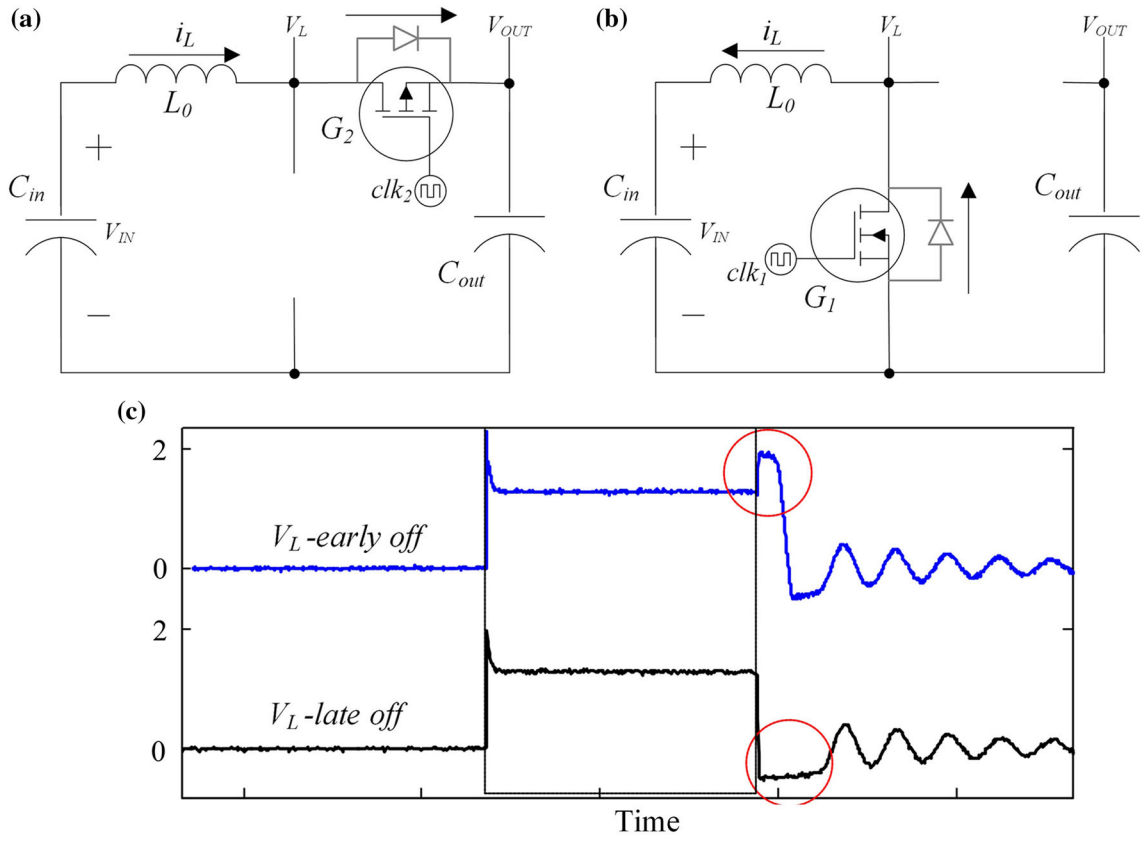

Fig. 8. Equivalent circuits and waveforms when G_2 is turned off too early/late. (a) Equivalent circuit when G_2 is turned off too early. (b) Equivalent circuit when G_2 is turned off too late. (c) Waveforms of V_L when G_2 is turned off too early or too late.

where f denotes the operation frequency of the boost converter.

Another type of power dissipation is the switching loss. When the switch G_1 is turned off, the converter starts to switch from "charge phase" to "discharge phase", and the inductor current reaches the peak value I_p. During the phase switching, there is a significant voltage-current overlap, which causes extra power dissipation in each cycle. The phase change can be divided into three stages as shown in Fig. 12. The current path and V–I overlap waveform are shown in Fig. 12a and b. The waveforms during the switching are shown in Fig. 9c.

The power loss during the turn-off procedure of switch G_1 is

$$P_{G1\_off} = \frac{1}{2} \cdot I_p \cdot (V_{OUT} + V_{PDS}) \cdot (T_1 + T_2) \cdot f \quad (10)$$

The power loss during the turn-on procedure of switch G_2 is

$$P_{G2\_on} = \frac{1}{2} \cdot I_p \cdot V_{PDS} \cdot (T_2 + T_5) \cdot f + I_p \cdot V_{PDS} \cdot (T_3 + T_4) \cdot f \quad (11)$$

The total switching loss is

$$P_{sw} = \frac{1}{2} \cdot I_p \cdot f \cdot [V_{PDS} \cdot (T_1 + 2T_2 + 2T_3 + 2T_4 + T_5) + V_{OUT} \cdot (T_1 + T_2)] \quad (12)$$

To simplify the calculation, it is assumed that the values of V_{PDS}, T_1, T_2, T_3, T_4 and T_5 are constant.

The power consumption of controller is also important to improve overall efficiency of the circuit, especially in low power energy harvesting circuit. From Fig. 6, the power consumption for MCU in one operational period is

$$P_{CU} = V_{CC} \cdot (i_{active} \cdot t_0 + i_{lpm3} \cdot t_1 + i_{lpm1} \cdot t_2 + i_{lpm4} \cdot t_3) \cdot f \quad (13)$$

where i_{active}, i_{lpm3}, i_{lpm2} and i_{lpm4} denote the current consumption of MCU during different operation modes.

In phase 3, the voltage of input capacitor is recharged from TEG output voltage through switch G_0. Therefore, t_3 can be calculated by

$$\frac{V_{IN} \cdot t_3 \cdot (V_T - V_{IN})}{R_T} = \frac{I_p^2 \cdot L}{2} \quad (14)$$

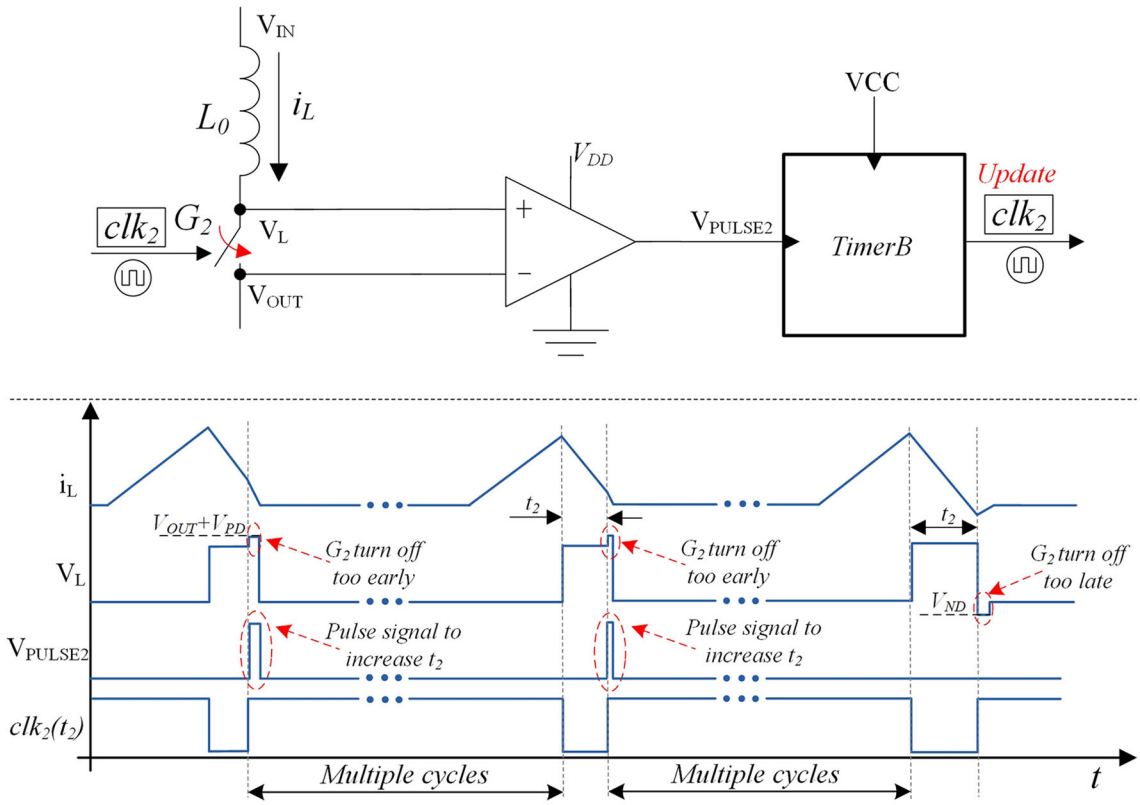

Fig. 9. Circuit diagram and operation process of the ZCS block.

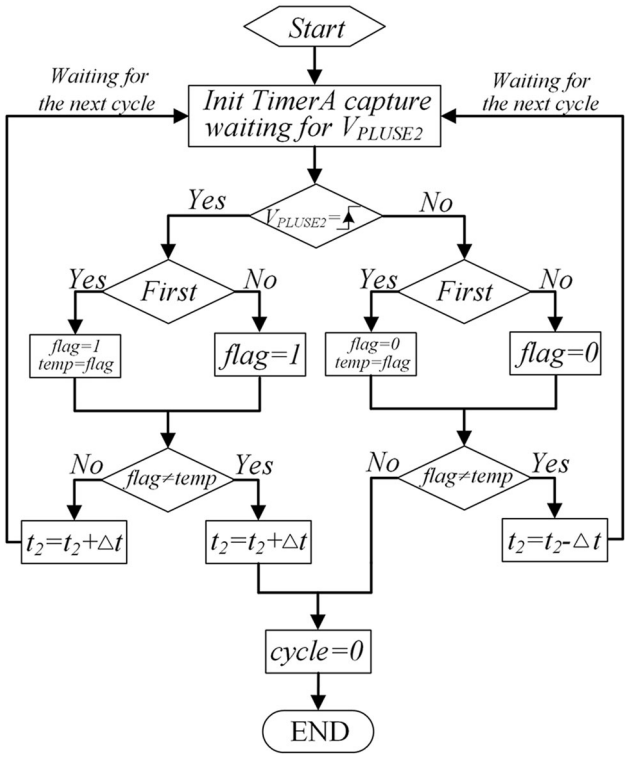

Fig. 10. Flow chart diagram for ZCS loop.

It is assumed that V_{IN} equals to half of V_T. There is

$$t_3 = \frac{L \cdot R_T \cdot I_p^2}{2V_{IN}^2} \tag{15}$$

In this design, t_3 is much longer than t_2 and t_1. There is

$$f = \frac{1}{t_3} = \frac{2V_{IN}^2}{L \cdot R_T \cdot I_p^2} \tag{16}$$

From Eqs. 13 and 16, there is

$$P_{CU} = 2.99 \times 10^{-6} + \frac{1.44 \times 10^{-5} \times V_{IN}^2}{I_p^2 \cdot L \cdot R_T} + \frac{1.38 \times 10^{-5} \times V_{IN}^2}{I_p \cdot R_T} + \frac{1.38 \times 10^{-3} \times V_{IN}^2}{I_p \cdot L \cdot V_{OUT}} \tag{17}$$

Current Control Scheme

The maximum output power of TEG is calculated by Eq. 1. The efficiency is

$$\eta = 1 - \frac{P_{CN} + P_{SW} + P_{CU}}{P_{in}} \tag{18}$$

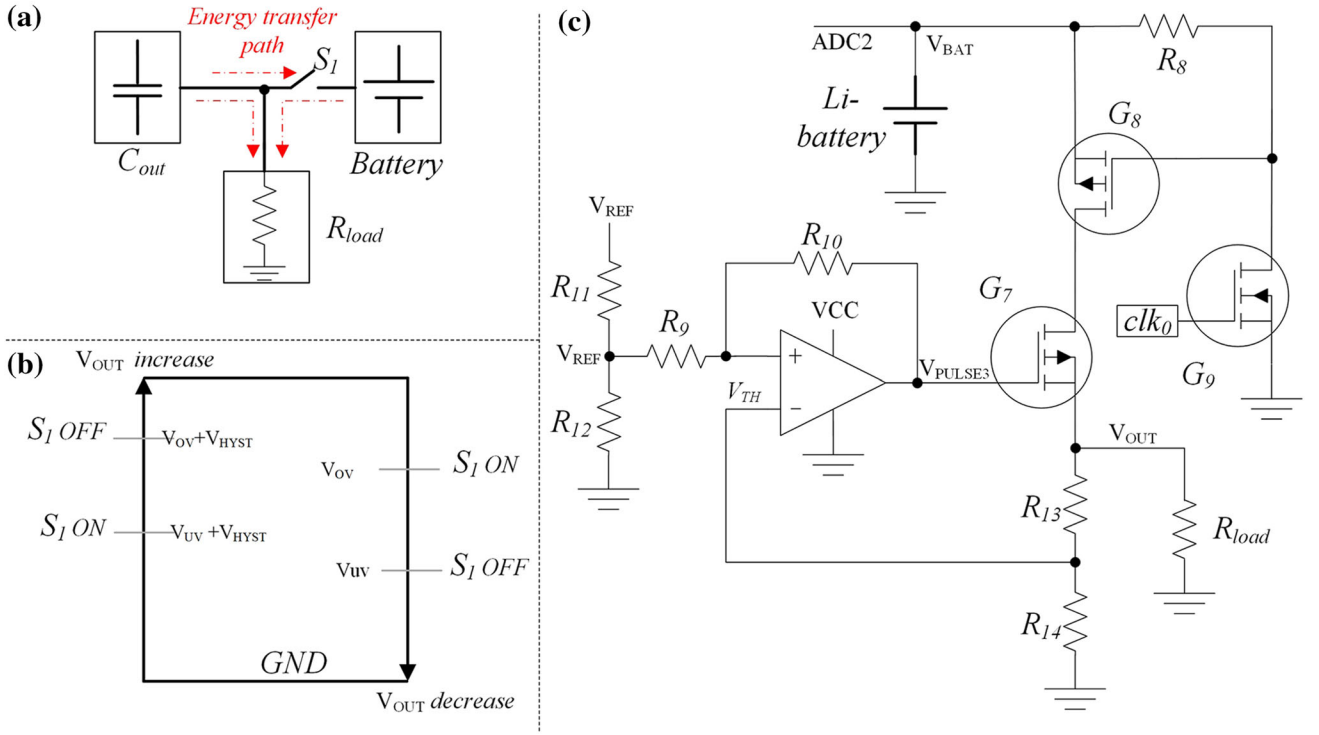

Fig. 11. Circuit diagrams and schematics of power management unit. (a) Simplified energy transfer path. (b) Summary of threshold voltages. (c) Detail of power management circuit.

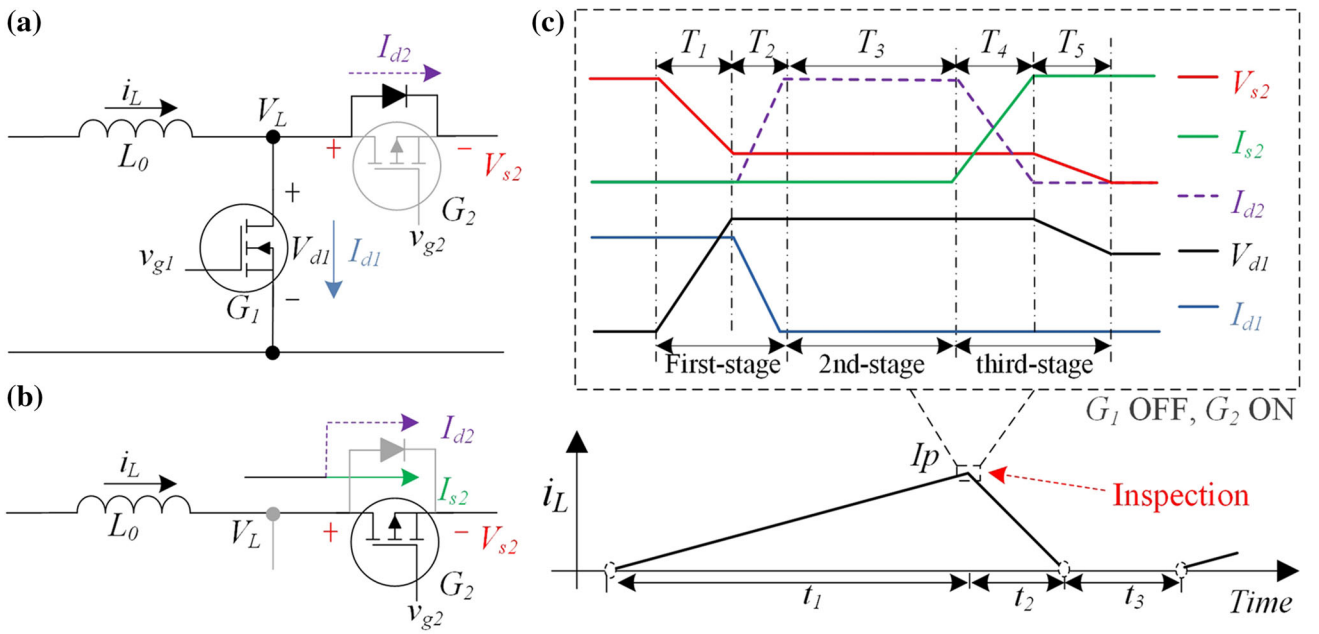

Fig. 12. Circuit analysis in the phase changing. (a) Circuit analysis in the first stage and second stage. (b) Circuit analysis in the third stage. (c) *V–I* overlap waveform during the switching.

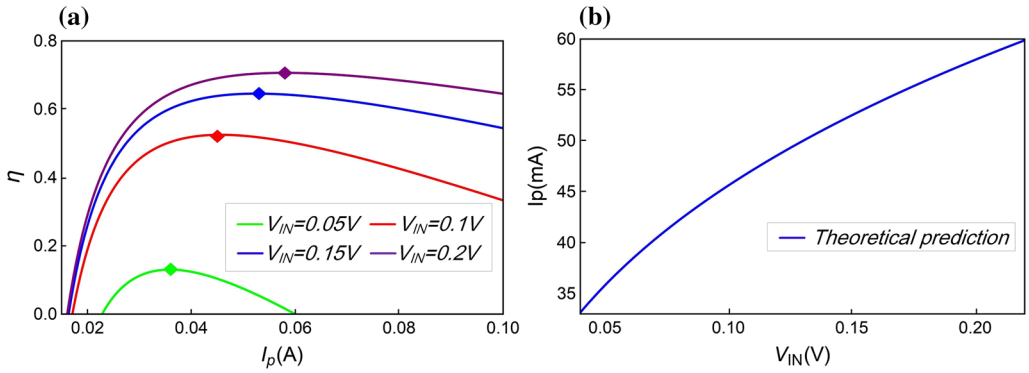

Fig. 13. The relationship between efficiency, I_p and V_{IN}. (a) Efficiency versus I_p with different V_{IN}, (b) Optimal I_p versus V_{IN}.

Table I. Components and circuit parameters

Component	Part number	Parameters
NMOS	WNM4153	R_{ON} = 0.15–0.21 Ω
PMOS	BSS215P	R_{ON} = 0.18–0.3 Ω
Inductor	TSL1315	0.68 mH, R_{DC} = 0.6 Ω
Comparator	TS881	I_{CC} = 210 nA, T_{PLH} = 5.1 μs, T_{PHL} = 6 μs
C_{in}	AVX	22 mF, ESR = 170 mΩ@1 K
C_{out}	–	100 μF
Supercapacitor	SCMR18F105	1 F

In this design, the value for L, R_L, R_{on1}, R_{on2}, R_T, and V_{OUT} are 680 μH, 0.6 Ω, 0.2 Ω, 0.2 Ω, 208 Ω, and 2.3 V, respectively. There is

$$\eta = \frac{1}{LV_{OUT}V_{IN}^2I_p^2} \times \begin{pmatrix} I_p^2L(V_{IN}^2 - 2.99\times10^{-6}R_T)V_{OUT} - 1.31\times10^{-7}V_{OUT}V_{IN}^2 \\ -I_pV_{IN}\begin{pmatrix} L(1.38\times10^{-3}V_{IN} + 9.2\times10^{-6}V_{OUT}) \\ +(1.2\times10^{-6} + 2\times10^{-7}V_{OUT})V_{OUT}V_{IN} \end{pmatrix} \\ -LV_{IN}I_p^3(0.67V_{IN}(R_L+R_{on1}) + 0.67V_{OUT}(R_L+R_{on2})) \end{pmatrix} \quad (19)$$

From Eq. 19, it is found that the efficiency is a function of I_p and V_{IN}. To provide an intuitive understanding of the relation between the efficiency and I_p, Eq. 19 is plotted as shown in Fig. 13a. From Fig. 13a, it is shown that the efficiency varies with I_p, and for different V_{IN}, optimal I_p is different for the highest efficiency. Then the optimal I_p was plotted as a function of V_{IN} and shown in Fig. 13b. Equation 4 can be rewritten as

$$t_1 = \frac{I_pL}{V_{IN} - i_L(R_L + R_{on1})} \quad (20)$$

Therefore, the optimal t_1 for the optimal I_p can be calculated for the system. In our designed system, based on the optimal current control scheme, the controller periodically detects the input voltage and generates the optimal t_1 for the highest efficiency.

EXPERIMENTS

Prototype and Experimental Setup

Based on the design schemes described in the previous section, the prototype system is built based on the off-the-shelf components. The circuit parameters are listed in Table I and the prototyped energy harvesting system is shown in Fig. 14. A commercial TEG modeled MPG-D655 from Micropelt Co. is used as the thermoelectric generator, which has an internal resistance of 208 ohms and a Seebeck coefficient of about 78 mV/°C. The hot side of the TEG is mounted on the heater (Modeled IKA C-MAC HP 7). The cold side of the TEG is clamped with a heat sink cooled by an open-loop water cooling system. Two thermocouples are tightly attached to the hot and cold sides of the TEG by thermal conductive paste to measure the temperatures. The temperature and voltage data are recorded by a data acquisition unit (Modeled Keysight 34972A).

MPPT, ZCS and PMU

According to the MPPT algorithm described in the "Circuit Architecture and Design Techniques" section, the performance of MPPT algorithm at different input voltage is examined. The steady-state waveforms of the input voltage V_{IN}, control signals clk_1, clk_2 and wake-up signal V_{PULSE1} under a minimum input voltage condition are shown in

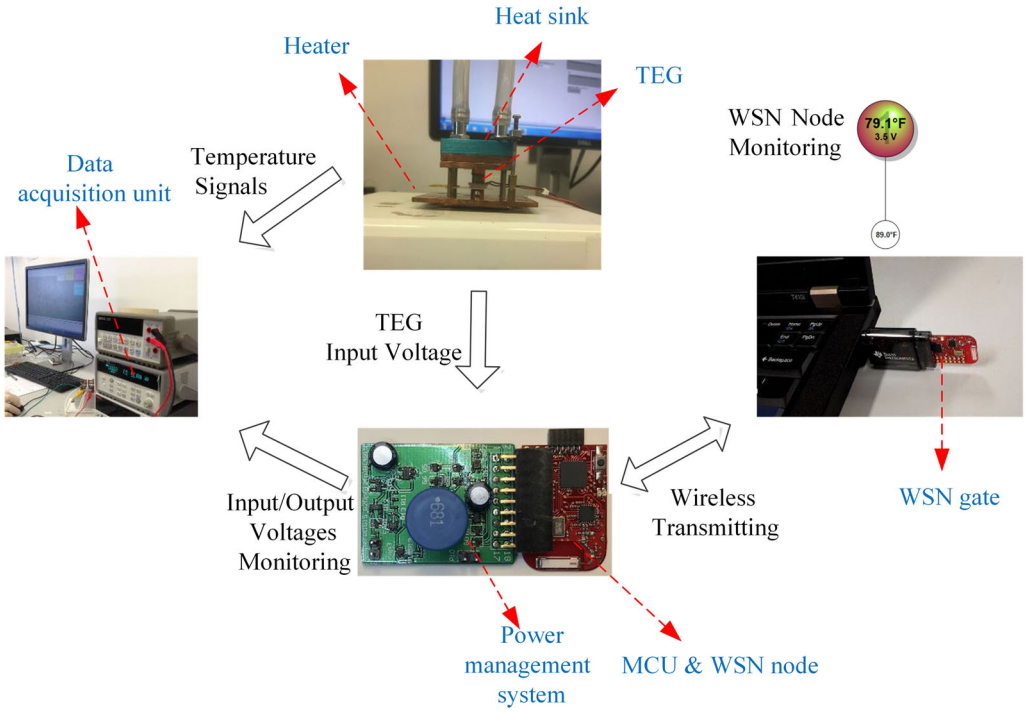

Fig. 14. Energy harvesting system prototype and experimental setup.

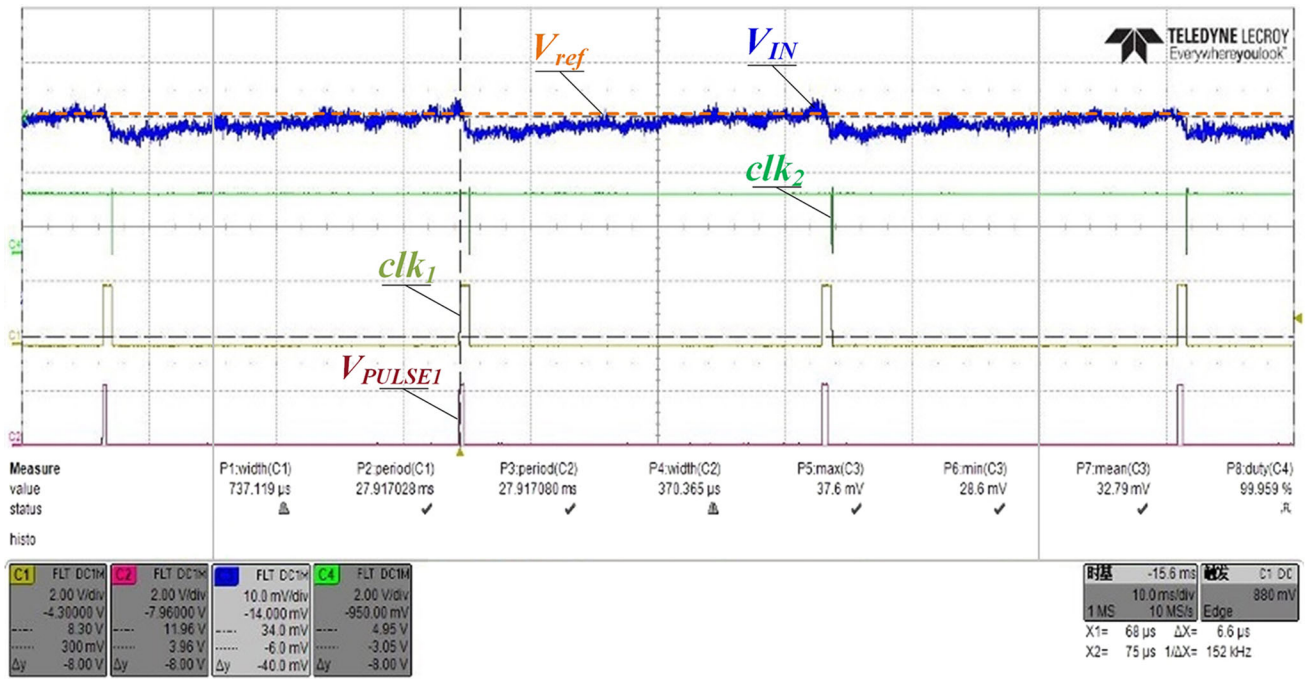

Fig. 15. Waveforms to show maximum power point tracking (V_{OC} = 80 mV, V_{IN} = 32.8 mV).

Fig. 15. From the figure, it is found that the waveforms match the analysis described in the "Maximum Power Extraction Based on DC–DC Converter" section.

During the experiments, the hot side temperature of the TEG ranges from 33.6°C to 34.2°C and the cold side temperature ranges from 27.7°C to 32.4°C. The corresponding output voltage of the TEG

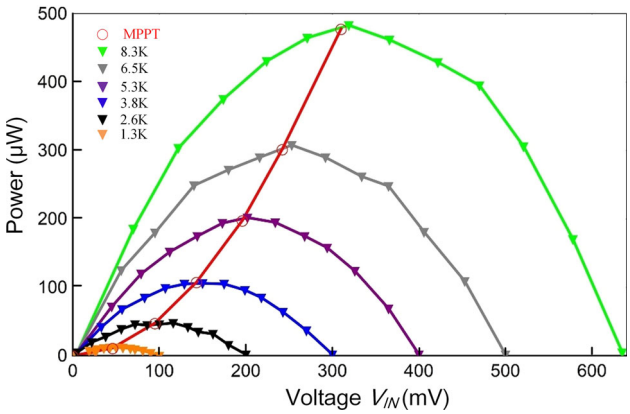

Fig. 16. The measured power versus the recorded input voltage at different load with different temperature difference (R_T = 208 Ω).

ranges from 100 mV to 640 mV. At each temperature difference, V_{IN} is recorded when the potentiometer is gradually adjusted from 5 Ω to 10 KΩ. For each load resistance, the power output can be calculated for temperature difference ranging from 1.3 K to 8.3 K. The triangle marked curve represents the measured power at various temperature differences.

Further, experiment is explored to verify the performance of the MPPT block as shown in Fig. 16. The red circle represents the input power P_{in} at each temperature difference. It is calculated that the MPPT scheme in the designed system can track the maximum power point with a high accuracy above 98%.

The experimental results of ZCS scheme are shown in Figs. 17 and 18. Under steady-state

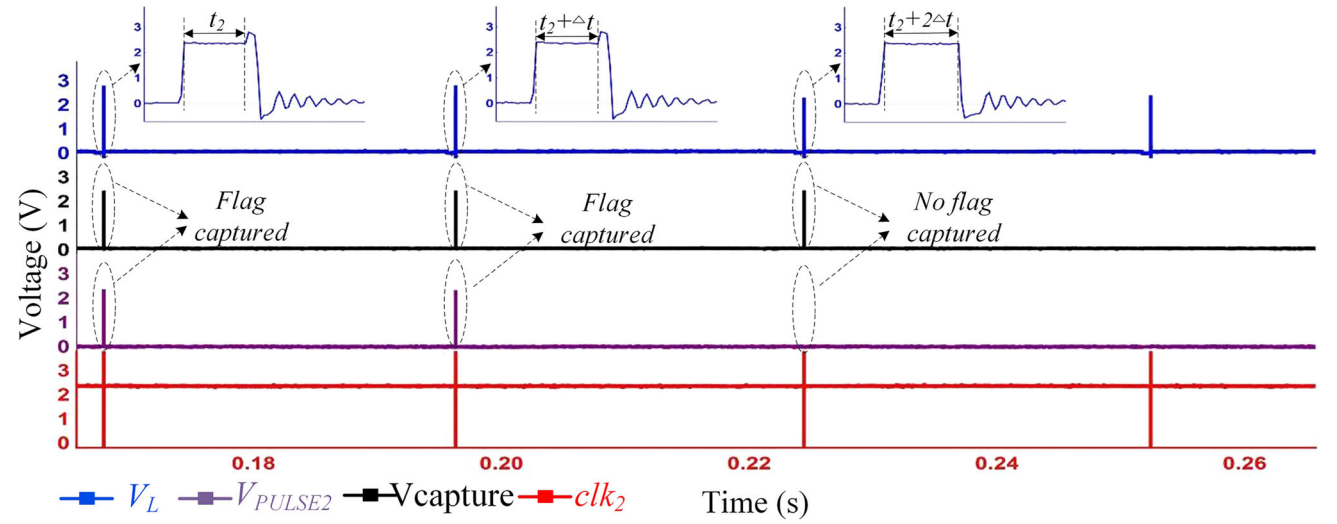

Fig. 17. The waveforms to show the ZCS procedure when t_2 is too short.

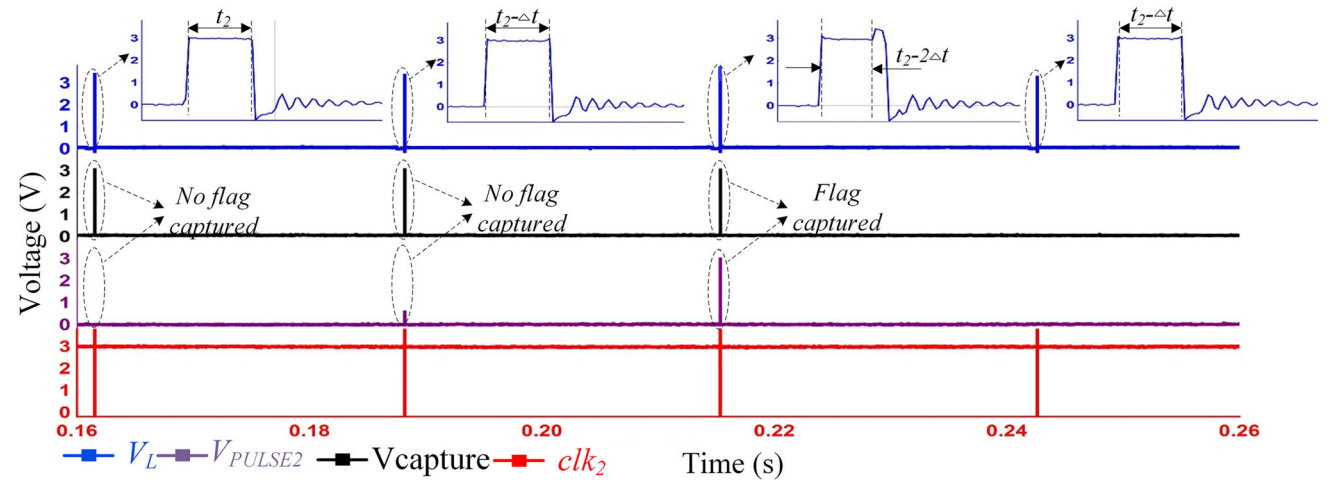

Fig. 18. The waveforms to show ZCS procedure when t_2 is too long.

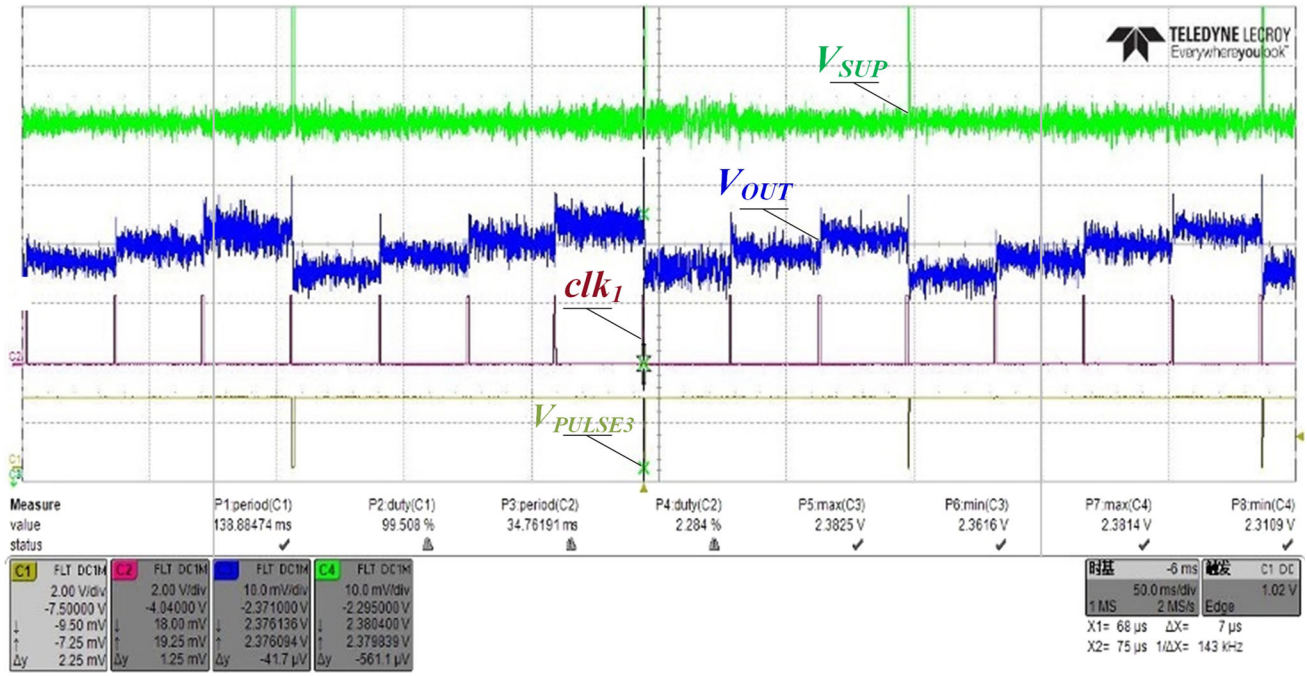

Fig. 19. Experimental waveforms of V_{SUP}, V_{OUT}, clk_1, and V_{PULSE3}.

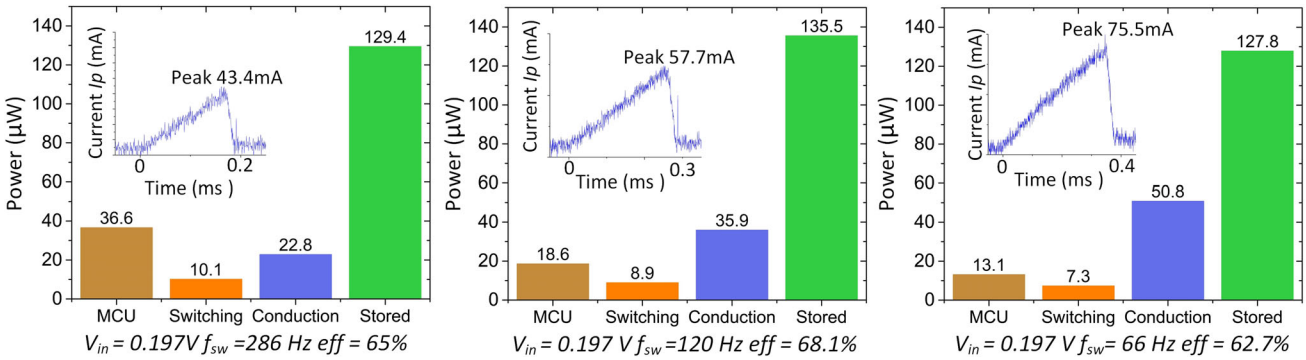

Fig. 20. Power consumption under different values of I_p (V_{IN} = 197 mV, R_T = 206 Ω), and the corresponding waveform of I_p shown in the inset.

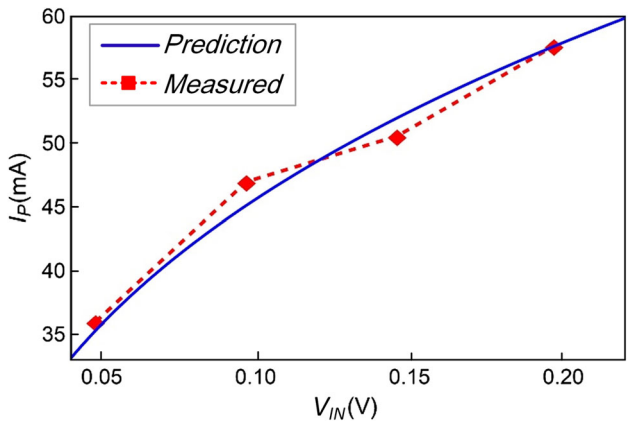

Fig. 21. Comparison of experimental and theoretical optimal I_p.

operation, the operation procedure of ZCS techniques is observed with an oscilloscope.

When the time interval t_2 is shorter than the optimal value, the adjusting procedure is shown in Fig. 17. First, signal V_{PULSE2} goes high after G_2 is turned off due to V_L is higher than V_{OUT}. Then V_{PULSE2} is captured by MCU, and t_2 is increased by Δt. Next, the value of t_2 continues to increase until no V_{PULSE2} signal is captured by MCU. The corresponding waveform is coincided with the analysis in the "ZCS Technique" section. Similarly, when the time interval t_2 is longer than the optimal value, the adjusting procedure is shown in Fig. 18.

Next, the operating procedure of the PMU is examined. The steady-state waveforms of the gate drive signal clk_1, supercapacitor voltage V_{SUP}, capacitor voltage V_{OUT}, and the voltage V_{PULSE3}

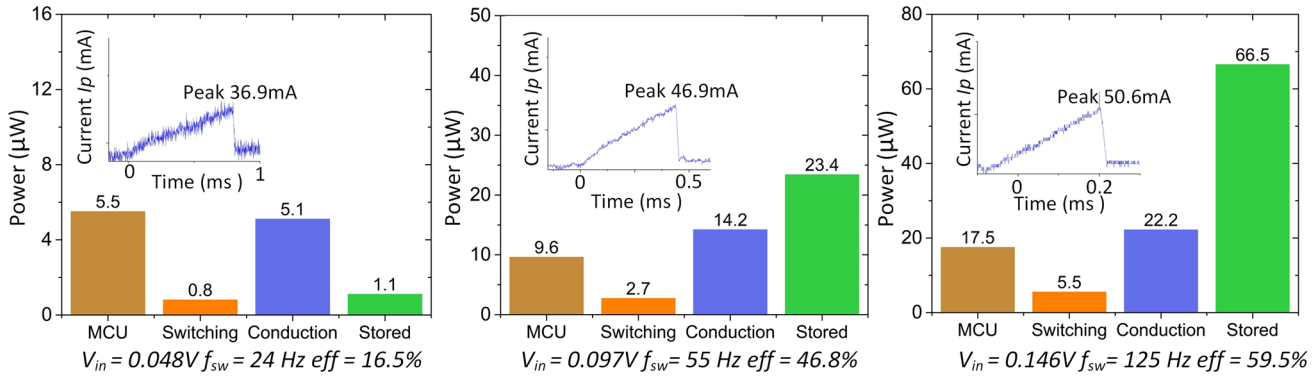

Fig. 22. Power consumption and stored power for different input voltages, and the corresponding waveform of I_p shown in the inset.

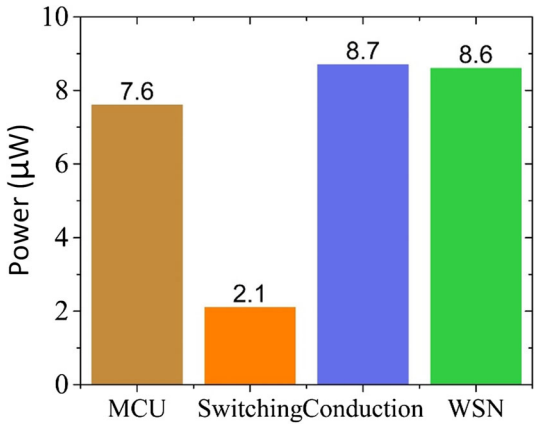

Fig. 23. Power consumption of the system with a WSN node.

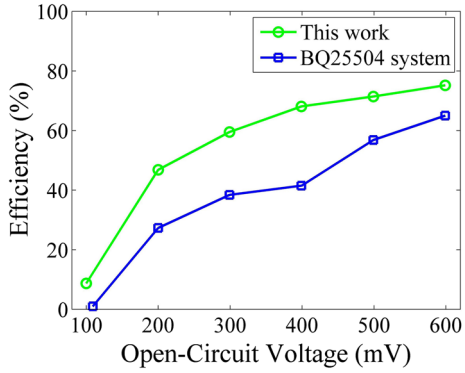

Fig. 24. Efficiency versus open-circuit voltage.

are shown in Fig. 19. The waveforms match the operation procedure of power management unit described in the "Power Management Strategy" section. Note that when the voltage V_{OUT} reached the threshold value $V_{UV} + V_{HYST}$ predefined by the external resistors, the voltage V_{OUT} decreased and V_{SUP} had a small increase. The energy on the capacitor is transferred to the supercapacitor.

Optimal Peak Current I_p and Breakdown of Losses

Experiments are explored to verify the analysis of optimal peak current I_p. A bar chart representing different power consumption and stored power is shown in Fig. 20. In Fig. 20, when I_p is 57.7 mA, the total power consumption is minimized, and the maximum efficiency is reached. In addition, it is noteworthy that MCU power consumption and switching power loss are gradually reduced with the decreasing of operation frequency f. On the other hand, the conduction loss increases. The experimental optimal peak inductor current I_p for the highest efficiency is shown as dot line in Fig. 21, compared with theoretical prediction shown in blue solid line. The difference between these two curves is less than 5%.

The power consumption and stored power at different input voltages of 48 mV, 97 mV, and 146 mV, respectively, are shown in Fig. 22. For each case, the system is working with optimal conductor current. It is shown that in the case of V_{IN} = 48 mV and P_{in} = 12.5 μW, the MCU is the major loss source. In the case of V_{IN} = 146 mV, the inductor conduction loss becomes the primary loss. It is found that when the input power is low, it is better to operate the converter in a lower frequency in order to reduce the power consumption of the control unit.

System Efficiency and Comparison

The experimental results show that when the transmission cycle of wireless transmitter is set as 30 s, the lowest open-circuit voltage for the system to be self-powered is 150 mV, and the lowest input power is 27 μW, with the corresponding temperature difference of 1.9 K. Under that working condition, the power consumption and stored power of the system are shown in Fig. 23.

To measure the system efficiency, a changeable load resistor is connected to the output of the boost converter with an output voltage of 2.3 V. The whole system efficiency is measured and plotted in Fig. 24 as the circle marked curve. It is shown that the efficiency ranges from 8.7% to 75.2% in the open-

circuit voltage ranging from 102 mV to 602 mV. Although a direct and fair comparison with other systems is difficult because of the different targeted power and operating condition, it may be worth comparing our system with the system of the commercial chip BQ25504 from TI Co. A converter system based on the BQ25504 commercial chip is built for comparison. The experimental efficiency based on BQ25504 towards the same voltage range is measured, as shown in the square-marked curve in Fig. 24. It is shown that the proposed energy harvesting system efficiency is higher than BQ25504 converter in the considered voltage range. The improvement may come from the optimal current scheme, MPPT and ZCS schemes, which are applied to reduce the power dissipation of the system.

CONCLUSIONS

A design of thermoelectric energy harvesting system integrated with a WSN node under low temperature difference condition is presented in this paper. High internal resistance TEG is used to harvest the thermoelectric energy. An MPPT scheme, a ZCS scheme and an optimal inductor current scheme are applied to increase the efficiency of the energy harvesting system.

Experimental results indicate that the proposed system can harvest power that ranges from 7.5 μW to 500 μW using the high internal resistance TEG. When the WSN node sends signals every 30 s, the lowest power for the energy harvesting system and the WSN node to be self-powered is 27 μW, with a temperature difference of 1.9 K. Experimental results show that the system can achieve a maximum efficiency of 75.2% at the temperature difference of 8 K and has a better efficiency than the commercial chip BQ25504. The circuit control strategy and low power design schemes in this paper can also be applied to other converter topologies such as buck and flyback converter.

ACKNOWLEDGMENTS

The work described in this paper was supported by grants from the China Science Foundation (Project Nos. 51777177, 51707168) and a grant from the Innovation and Technology Commission of Hong Kong Special Administrative Region, China (Project No. ITS/248/14FP).

REFERENCES

1. K. Romanjek, S. Vesin, L. Aixala, T. Baffie, G. Bernard-Granger, and J. Dufourcq, *J. Electron. Mater.* 44, 2192 (2015).
2. D. Jean-Marie, R. Monthéard, M. Bafleur, V. Boitier, P. Durand-Estèbe, and P. Tounsi, *J. Electron. Mater.* 43, 2444 (2014).
3. M. Thielen, G. Kara, I. Unkovic, D. Majoe, and C. Hierold, *J. Electron. Mater.* 47, 3307 (2018).
4. F. Deng, H. Qiu, J. Chen, L. Wang, and B. Wang, *IEEE Trans. Ind. Electron.* 64, 1477 (2017).
5. K.T. Settaluri, H. Lo, and R.J. Ram, *J. Electron. Mater.* 41, 984 (2012).
6. M. Guan, K. Wang, Q. Zhu, and W. Liao, *J. Electron. Mater.* 45, 5514 (2016).
7. M. Guan, K. Wang, D. Xu, and W. Liao, *J. Energy Convers. Manag.* 138, 30 (2017).
8. Micropelt, MPG-D655 Thin Film Thermogenerator datasheet (2014). http://www.micropelt.com/fileadmin/user_upload/_PDF_TGP_UK.pdf.
9. Tellurex, Tellurex Thermoelectric Energy Harvester-G1-1.0-127-1.27, datasheet (2011). http://educypedia.karadimov.info/library/termo.pdf.
10. Y. The and P.K.T. Mok, *IEEE J. Solid State Circuits* 49, 2694 (2014).
11. Z. Jorge, C. Salvador, C. Alfredo, and S. Edgar, *IEEE Trans. Circuits Syst.* 62, 1918 (2015).
12. Texas Instruments, BQ25504 datasheet (2018). http://www.ti.com/lit/ds/symlink/bq25504.pdf.
13. Linear Technology, LTC 3108 datasheet (2010). http://cds.linear.com/docs/en/datasheet/3108fc.pdf.
14. Texas Instruments, EZ430-RF2500 datasheet (2012). http://www.ti.com/lit/ug/slau227f/slau227f.pdf.